

# No evidence for bilinear condensate in parity-invariant three-dimensional QED with massless fermions

Nikhil Karthik\* and Rajamani Narayanan†

*Department of Physics, Florida International University, Miami, FL 33199.*

(Dated: September 24, 2018)

## Abstract

We present our numerical study of three-dimensional QED with 2, 4, 6 and 8 flavors of massless two-component fermions using a parity-preserving lattice regularization with Wilson fermions. We study the behavior of low-lying eigenvalues of the massless improved Wilson-Dirac operator as a function of three-dimensional physical volume, after taking the continuum limit at fixed physical volumes. We find the following evidences against the presence of bilinear condensate: the eigenvalues do not scale as the inverse of the three-dimensional physical volume, and the number variance associated with these eigenvalues do not exhibit ergodic behavior. The inverse participation ratio (IPR) of the associated eigenvectors exhibits a multi-fractal volume scaling. The relation satisfied by number variance and IPR suggests critical behavior.

PACS numbers: 11.15.Ha, 11.10.Kk, 11.30.Qc

arXiv:1512.02993v3 [hep-lat] 4 Feb 2016

---

\* nkarthik@fiu.edu

† rajamani.narayanan@fiu.edu

## I. INTRODUCTION

Two component massless fermions coupled to a three-dimensional Euclidean abelian gauge field has been a topic of study in the past three decades for several field-theoretic reasons, and it is also of interest to condensed matter physics [1]. The massless Dirac operator is

$$\mathcal{C}(\mathbf{A}) = \sum_{k=1}^3 \sigma_k [\partial_k + iA_k(\mathbf{x})], \quad (1)$$

where  $\sigma_k$  are the Pauli matrices and  $A_k(\mathbf{x})$  is a background abelian field. Under parity,

$$\mathbf{x} \rightarrow -\mathbf{x}; \quad \mathbf{A}(\mathbf{x}) \rightarrow -\mathbf{A}(-\mathbf{x}); \quad \mathcal{C}(\mathbf{A}) \rightarrow \mathcal{C}^\dagger(\mathbf{A}) = -\mathcal{C}(\mathbf{A}). \quad (2)$$

This theory has a parity anomaly [2, 3] since the fermion determinant is not real [4, 5] and its parity-violating phase is regulator dependent [6–8]. Furthermore, the form of the parity-violating term at finite temperature and non-trivial gauge field backgrounds can be quite different from the perturbative infinite volume result [9, 10].

This parity anomaly can be cancelled by suitable regularization when even number of flavors of two-component fermions are present. In this paper, we are only interested in such a system. Assuming we have a regulated version of  $\mathcal{C}(\mathbf{A})$ , we can write down a parity invariant fermionic action for a  $2N_f$  flavor theory as

$$S_f = \int d^3x \sum_{i=1}^{N_f} \{ \bar{\chi}_i(\mathbf{x}) \mathcal{C}(\mathbf{A}) \chi_i(\mathbf{x}) + \bar{\phi}_i(\mathbf{x}) \mathcal{C}^\dagger(\mathbf{A}) \phi_i(\mathbf{x}) \}, \quad (3)$$

with the fermions transforming under parity as

$$\bar{\chi}_i(\mathbf{x}) \rightarrow \bar{\phi}_i(\mathbf{x}); \quad \chi_i(\mathbf{x}) \rightarrow \phi_i(\mathbf{x}). \quad (4)$$

It is useful to identify the  $2N_f$  flavors of 2-component fermions as  $N_f$  flavors of 4-component fermions using the following notation [11],

$$\psi_i(\mathbf{x}) = \begin{pmatrix} \phi_i(\mathbf{x}) \\ \chi_i(\mathbf{x}) \end{pmatrix}; \quad \bar{\psi}_i(\mathbf{x}) = \left( \bar{\chi}_i(\mathbf{x}) \quad \bar{\phi}_i(\mathbf{x}) \right); \quad \mathcal{D}(\mathbf{A}) = \begin{pmatrix} 0 & \mathcal{C}(\mathbf{A}) \\ \mathcal{C}^\dagger(\mathbf{A}) & 0 \end{pmatrix}, \quad (5)$$

with the associated action,

$$S_f = \int d^3x \sum_{i=1}^{N_f} \bar{\psi}_i(\mathbf{x}) \mathcal{D}(\mathbf{A}) \psi_i(\mathbf{x}). \quad (6)$$

Note that the usual anti-hermitian Dirac operator is

$$\gamma_5 \mathcal{D}(\mathbf{A}) = \sum_{k=1}^3 \gamma_k [\partial_k + iA_k(\mathbf{x})]. \quad (7)$$

Under parity,

$$\psi_i(\mathbf{x}) \rightarrow P\psi_i(\mathbf{x}); \quad \bar{\psi}_i(\mathbf{x}) \rightarrow \bar{\psi}_i(\mathbf{x})P; \quad P = \begin{pmatrix} 0 & 1 \\ 1 & 0 \end{pmatrix}; \quad \mathcal{D}(\mathbf{A}) \rightarrow P\mathcal{D}(\mathbf{A})P = -\mathcal{D}(\mathbf{A}). \quad (8)$$

The action in Eq. (6) has a  $U(2N_f)$  symmetry. The two fermion bilinears which break the symmetry to  $U(N_f) \times U(N_f)$ , but invariant under parity, are

$$S_m = \int d^3x [m_p \bar{\psi}_i(\mathbf{x}) P \psi_i(\mathbf{x}) + im \bar{\psi}_i(\mathbf{x}) \psi_i(\mathbf{x})]. \quad (9)$$

The fermion determinant in a fixed gauge field background becomes

$$Z(m, m_p) = \det (\mathcal{C}(\mathbf{A})\mathcal{C}^\dagger(\mathbf{A}) + m^2 + m_p^2), \quad (10)$$

which makes different choices of  $m$  and  $m_p$  equivalent as long as  $m^2 + m_p^2$  remains the same. These different ways to introduce mass will be used advantageously in our lattice formulation. If the  $U(2N_f)$  symmetry gets spontaneously broken to  $U(N_f) \times U(N_f)$  in the massless theory, then  $\bar{\psi}_i \psi_i$  and  $\psi_i P \psi_i$  will pick a vacuum expectation value, which we refer to as the bilinear condensates. With the right ordering of limits (the three-dimensional volume  $\ell^3$  is taken to infinity before the fermion mass is taken to zero), the bilinear condensates are

$$\lim_{m \rightarrow 0} \lim_{\ell \rightarrow \infty} \frac{1}{\ell^3} \frac{\partial \log \langle Z(m, 0) \rangle}{\partial m} \neq 0 \quad \text{and} \quad \lim_{m_p \rightarrow 0} \lim_{\ell \rightarrow \infty} \frac{1}{\ell^3} \frac{\partial \log \langle Z(0, m_p) \rangle}{\partial m_p} \neq 0. \quad (11)$$

Analytic arguments in favor of a non-zero bilinear condensate were first provided by Pisarski [11] in the limit of large number of flavors. The associated gap equation was analyzed in [12–15] which supports a non-zero bilinear condensate if  $N_f < 4$ . It is worthwhile noting that the massless fermion propagator was used in the fermion bubbles summed up to obtain the gauge boson propagator. In addition, the wave function renormalization of the fermion was set to unity in the limit of large  $N_f$ . Since the computation was performed in the large- $N_f$  limit and an upper bound on  $N_f$  was obtained for a non-zero bilinear condensate, a different approach is needed to verify this result. Furthermore, estimating the free energy by simply counting the degrees of freedom in the UV and IR assuming a non-zero bilinear condensate suggests a bound

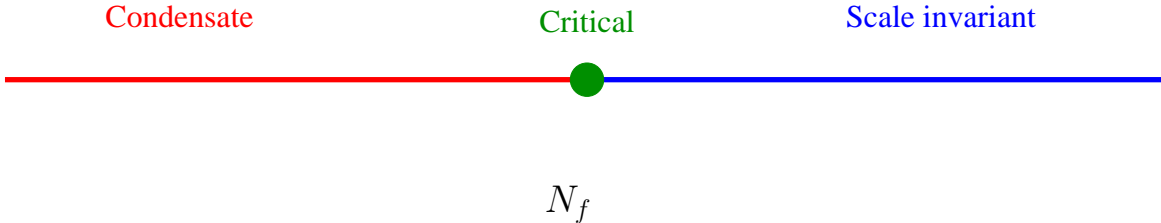


FIG. 1. The conjectured phase diagram of three-dimensional QED as a function of the number of flavors  $N_f$  of massless 4-component fermions. The blue region (to the right of critical point) has a  $U(2N_f)$  flavor symmetry and scale invariance. The symmetry is broken to  $U(N_f) \times U(N_f)$  in the red region (to the left of the critical point). This paper deals with whether this region with bilinear condensate (and broken scale invariance) exists.

of  $N_f < 2$  [16]. In another study [17], the stability of the conformal fixed point of QED in  $4 - \epsilon$  dimensions on a sphere, extrapolated to three dimensions, suggests a critical  $N_f < 4$ . A schematic phase diagram of  $\text{QED}_3$  as a function of the number of flavors is shown in Figure 1, based on the above plausibility arguments. The question we try to answer, is the existence of the region with condensate and broken  $U(2N_f)$  symmetry.

Extensive numerical studies have been carefully performed using staggered fermions to investigate the possibility of a non-vanishing bilinear condensate. A single copy of staggered fermion results in a  $N_f = 2$  theory in the continuum. This particular example was studied in [18] and an upper bound on the bilinear condensate was estimated. By simulating a lattice model that uses the square root of the staggered Dirac operator, the  $N_f = 1$  theory was carefully studied in [19] and concluded that there is evidence for a non-zero bilinear condensate in this theory. In these studies, the theory with a fermion mass was simulated and the bilinear was measured as a function of mass to see if an extrapolation to zero mass yielded a non-zero condensate in the infinite volume limit. Although several different physical volumes and lattice spacings were considered the analysis did not separate the two effects. In the  $N_f = 1$  case, increasing the physical volume at a fixed lattice spacing shows a trend in the bilinear as a function of mass, that is in favor of a non-zero condensate at zero mass. But, a comparison of two different physical volumes (the largest two in the simulation) at two different lattice spacings favors a vanishing condensate at zero mass. The  $N_f = 4$  theory was also studied in [19] with the aim of showing that the condensate vanishes in this theory. An equation of state analysis of the bilinear condensate as a

function of fermion mass and lattice gauge coupling does not convincingly provide evidence for a non-vanishing condensate at  $N_f = 1$  nor for a vanishing condensate at  $N_f = 4$ .

The aim of this paper is to revisit the problem numerically using Wilson fermions. The advantage of using Wilson fermions are two-fold. On the one hand, we can simulate any value of  $N_f$  without having to deal with fractional powers of the lattice Dirac operator. On the other, there is a place for both the bilinears in Eq. (9) — we use  $m_p$  on the lattice to realize massless fermions and use  $m$  to find evidence for a non-zero condensate. Wilson fermions were used earlier in [20] to study the beta function of QED<sub>3</sub> with  $N_f = 2$ ; here we use the two different masses to study  $N_f \geq 1$  and explore fermionic observables. In contrast to the studies in [18, 19] where one simulates a theory with a non-zero  $m$ , we simulate the theory with  $m = 0$  and study the behavior of the low-lying eigenvalues as a function of the physical volume. The low-lying eigenvalues were previously studied in the quenched approximation in [21]. Differing in the method, our study here explicitly extracts the scaling behavior of the low-lying eigenvalues with respect to the volume. In particular, we expect the lowest eigenvalues of  $\mathcal{D}(\mathbf{A})$ ,  $\lambda_i$ , in a box of volume  $\ell^3$ , to scale such that the expectation value of  $\lambda_i \ell^3 \Sigma$  has a finite non-zero limit as  $\ell \rightarrow \infty$  with  $\Sigma$  being the value of non-zero condensate.

The organization of the paper is as follows: we will present the parity-invariant formalism of Wilson fermions on the lattice in Section II. We will present our results for  $N_f = 1$  in Section III where we will also make contact with certain ideas in random matrix theory in order to understand the behavior of the low-lying modes of the improved Wilson-Dirac operator. We will present the results for  $N_f = 2, 3$  and 4 in Section IV, and compare them to the  $N_f = 1$  case. This will be followed by our conclusions.

## II. PARITY INVARIANT WILSON FERMIONS

We used an isotropic  $L^3$  lattice with periodic boundary conditions in all three directions. Following [18, 19], we used the non-compact gauge action given by

$$S_g = \frac{L}{\ell} \sum_n \sum_{j < k}^3 \left[ \theta_j(n) + \theta_k(n + \hat{j}) - \theta_j(n + \hat{k}) - \theta_k(n) \right]^2, \quad (12)$$

where  $\ell$  is the dimensionless linear extent of the periodic box measured in units of the coupling constant. The  $\theta$ 's are related to the gauge-fields as  $\theta_k = \frac{\ell}{L} A_k$ . We used the Sheikholami-Wohlert-Wilson-Dirac operator [22] which was improved further by using one-level HYP smeared fields

$\theta_k^s$  [23, 24] in the naive and Wilson terms. Let  $C_W$  denote the two component Sheikholeslami-Wohlert-Wilson-Dirac operator including the mass term  $M_P$ . We have given the details of smearing and  $C_W$  in Appendix A. In four component notation, our lattice realization of the continuum parity-invariant operator with mass terms (refer Eq. (6) and Eq. (9)) is

$$D_W = \begin{pmatrix} iM & C_W \\ C_W^\dagger & iM \end{pmatrix}. \quad (13)$$

The eigenvalues of  $D_W$  come in complex conjugate pairs:

$$D_W \phi_j^\pm = (iM \pm \Lambda_j(M_P)) \phi_j^\pm; \quad \phi_j^\pm = \frac{1}{\sqrt{2}} \begin{pmatrix} u_j \\ \pm \frac{1}{\Lambda_j(M_P)} C_W^\dagger u_j \end{pmatrix}, \quad (14)$$

where  $\Lambda_j$  are the eigenvalues of the massless Dirac operator in lattice units. In terms of the two-component Dirac operator,

$$C_W C_W^\dagger u_j = \Lambda_j^2(M_P) u_j; \quad \Lambda_j(M_P) > 0; \quad u_j^\dagger u_j = 1. \quad (15)$$

As  $L \rightarrow \infty$ , the massless limit is obtained by setting  $M = M_P = 0$ . Due to the additive renormalization of  $M_P$ , one needs to tune  $M_P$  as function of  $L$  in order to remain massless after setting  $M = 0$ .

The dimensionless bilinear condensate is given by

$$\Sigma = \frac{1}{\ell^2} \left\langle \sum_j \frac{2m\ell}{(\lambda_j \ell)^2 + (m\ell)^2} \right\rangle, \quad (16)$$

where the quantities in the continuum are

$$\lambda_j \ell = \lim_{L \rightarrow \infty} \Lambda_j(M_P) L \quad \text{and} \quad m\ell = \lim_{L \rightarrow \infty} M L. \quad (17)$$

Then, for  $\Sigma$  to be non-zero in the massless limit, we require the low-lying eigenvalues to obey [25, 26]

$$\lambda_j \ell = \frac{\Sigma z_j}{\ell^2}, \quad (18)$$

with  $z_j$  being certain universal numbers obtained from an appropriate random matrix theory that properly accounts for the effective low energy Lagrangian with only the zero momentum mode taken into account. This is an important requirement that we use to check if the bilinear condensate is present.

We explicitly set  $M = 0$  in our simulations. This enabled us to use the standard Hybrid Monte Carlo [27] algorithm with  $N_f$  copies of pseudofermions to simulate a  $2N_f$  flavor theory. We used

$M_P$  to tune the theory to massless fermions. The tuning was achieved by finding the  $M_P$  that minimizes the lowest eigenvalue,  $\Lambda_1(M_P)$ , over a small ensemble of thermalized configurations. We computed these low-lying eigenvalues, including the associated eigenvectors, using the Ritz algorithm [28]. Our simulation parameters are given in Appendix B.

### III. RESULTS FOR $N_f = 1$

#### A. Effective potential using Wilson loops

We start with the results for the effective potential by measuring the energy,  $-\log W(x, t)$ , of a rectangular Wilson loop,  $W$ , of size  $x \times t$ . We regularized the loop by spatially smoothening the gauge-fields  $\theta_1$  and  $\theta_2$  perpendicular to  $t$ , using 6 levels of APE smearing with the smearing parameter  $s = 0.5$ . By fitting to

$$\log(W) = A + V(x)t, \quad (19)$$

with  $A$  and  $V(x)$  as fit parameters, we obtained the effective potential,  $V(x)$ , which is shown in the top panel of Figure 2. A dominant  $\log(x)$  behavior is seen. The deviation from the  $\log(x)$  behavior that is seen at large  $x$ , diminishes as the physical volume is increased. A fit of the data to

$$V(x) = k \log(x), \quad (20)$$

shows that  $k$  approaches an infinite volume result. But,  $V(x)$  at a fixed  $x$ , does not seem to have a finite limit. Instead, the log-term seems to be of the form  $\log(\frac{x}{\ell})$ , as seen from the data collapse in the bottom panel of Figure 2. Therefore, the effective potential does have a three-dimensional Coulomb-like behavior but one cannot set a scale using the potential.

#### B. Scaling of low-lying eigenvalues with physical extent $\ell$

We turn our attention to the behavior of the lowest lying eigenvalues as a function of the box size  $\ell$ . In Figure 3, we show the lattice corrections to the smallest dimensionless eigenvalue,  $\lambda_1 \ell$ , at various physical volumes  $\ell^3$ . As it can be seen, the lattice corrections are small at all volumes and under control. Using a linear  $\frac{1}{L}$  extrapolation, we were able to obtain the continuum limit of the eigenvalues. Such continuum extrapolations for representative volumes are shown by the straight lines in Figure 3. We plot  $\lambda_1 \ell$  as a function of  $\ell$  for the four largest value of  $L$  in our

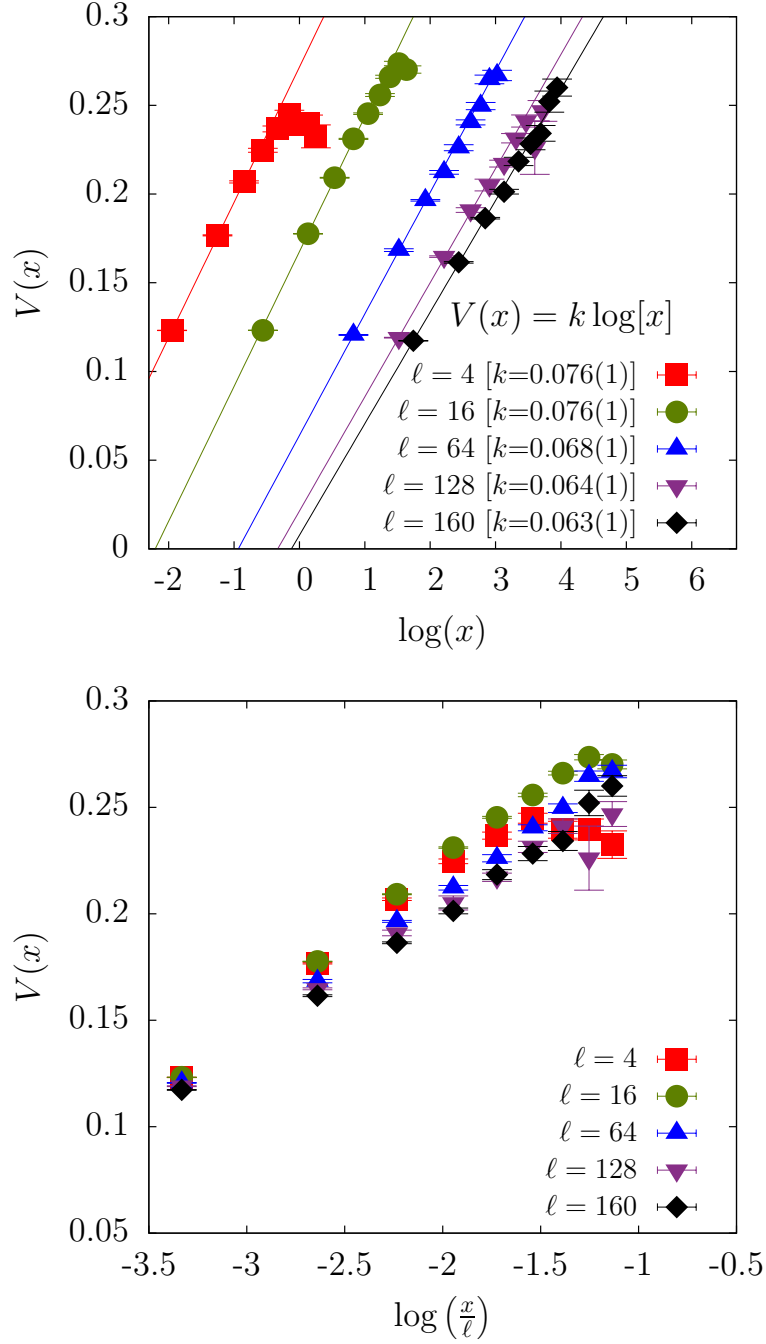


FIG. 2. The effective potential,  $V(x)$ , as a function of the separation,  $x$ , on several different physical volumes as obtained from  $x \times t$  Wilson loops. In the top panel,  $V(x)$  is plotted as a function of  $\log(x)$ . The straight lines are the best fits to  $V(x) = k \log(x)$ . In the bottom panel, it is plotted as a function of  $\log(x/\ell)$ . The data collapse suggests that one cannot set scale using the effective potential.



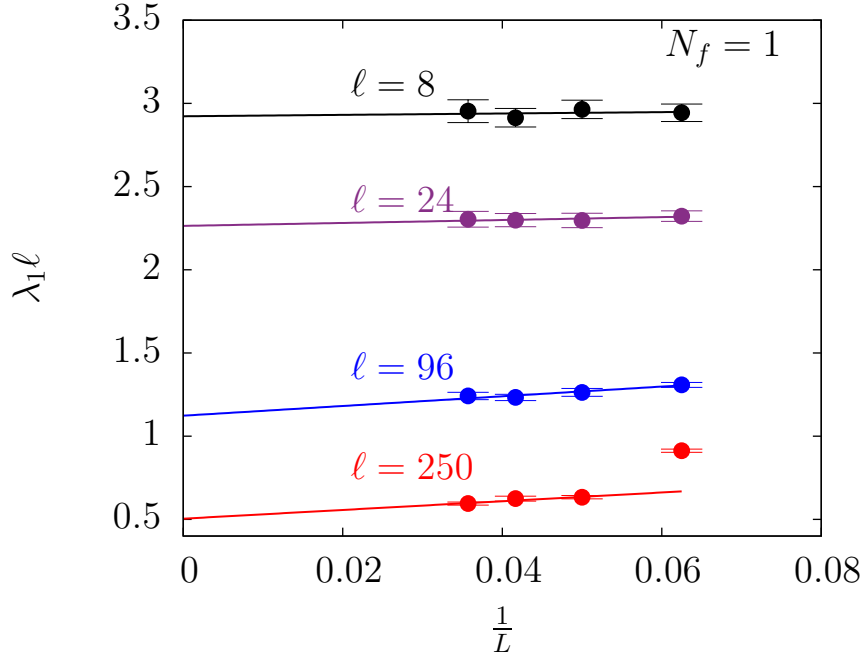


FIG. 3. Continuum limit of the lowest eigenvalue at various representative box sizes  $\ell$ . The straight lines are the continuum extrapolations using a linear  $\frac{1}{L}$  fit.

simulation in the top panel of Figure 4. In addition we also show the continuum limit in the same plot. We expect  $\lambda_1 \ell \sim \ell^{-2}$  if this theory has a non-zero bilinear condensate. The data shown in the log-log plot is not described by a simple linear fit. In the bottom panel of Figure 4, we compare the continuum extrapolated  $\lambda_1 \ell$  with a  $\ell^{-2}$  power-law. Large deviation from the  $\ell^{-2}$  behavior is seen at all volumes. To quantify this statement with some confidence, we fitted the lowest three eigenvalues to a rational ansatz

$$\log(\lambda \ell) = \frac{a_1 - \left(p + \frac{a_2}{\ell}\right) \log(\ell)}{1 + \frac{a_3}{\ell}}, \quad (21)$$

such that one recovers a power-law as  $\ell \rightarrow \infty$ . Using this, we extracted the leading power  $p$ . The best fit is shown as a solid blue curve in the bottom panel of Figure 4. The  $\chi^2/\text{DOF}$  as a function of  $p$  is shown in Figure 5. The value of  $p$  around 1 seems to be favored while the value  $p = 2$ , as expected when non-zero bilinear condensate is present, seems to be ruled out. The value of  $\chi^2$  seems to be minimized around the same value for all the low-lying eigenvalues, suggesting that they all scale the same way with  $\ell$ .

It is possible that our studies have not reached asymptotically large volumes. In fact such a possibility has been put forward in [29] by studying the effect of an infra-red cutoff on the gap

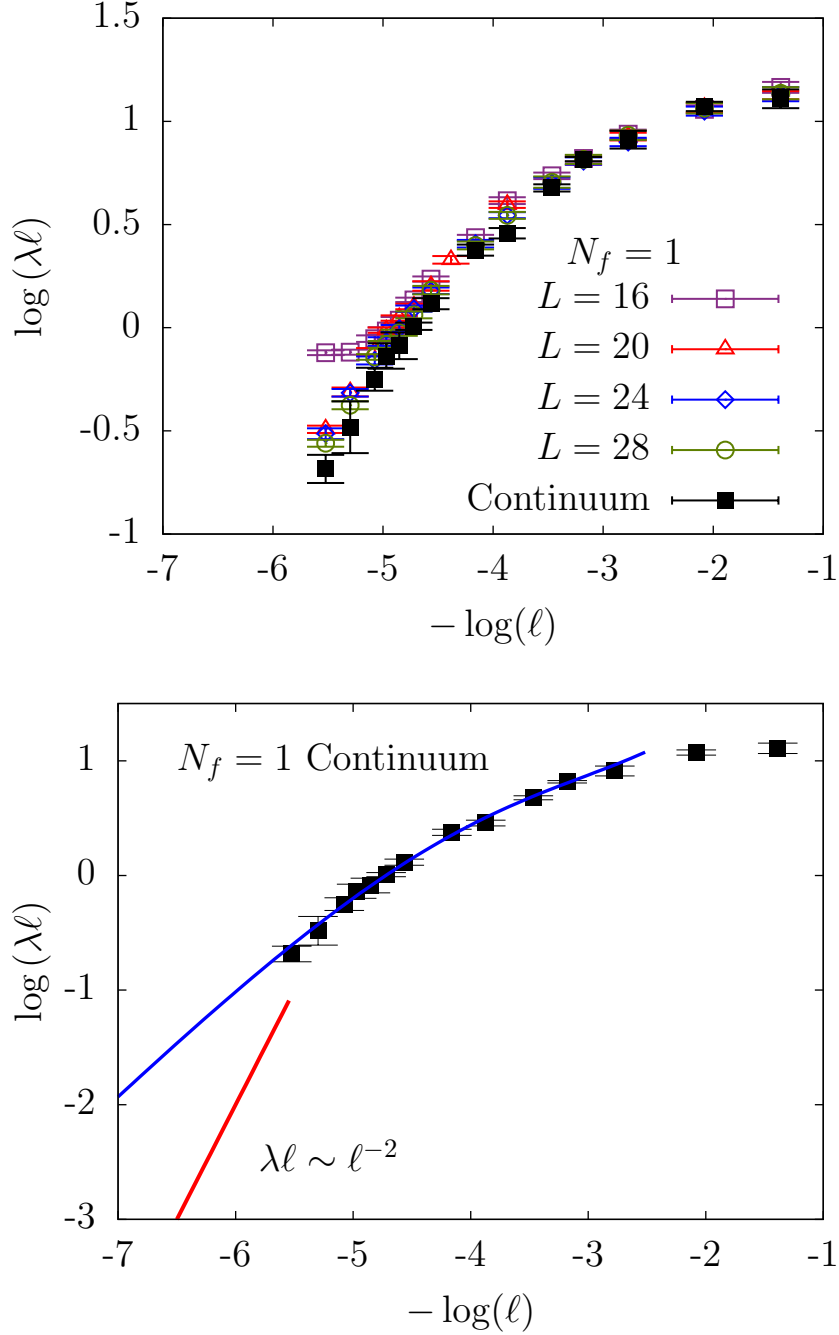


FIG. 4. The top panel shows the behavior of the lowest eigenvalue as a function of the physical volume at finite lattice spacing and in the continuum limit. The bottom panel compares the  $\ell$ -dependence of the lowest eigenvalue (in the continuum limit) with the expected behavior for a non-zero condensate (red straight line). The solid blue curve is the best fit using the finite volume ansatz in Eq. (21) with  $p = 1$ .

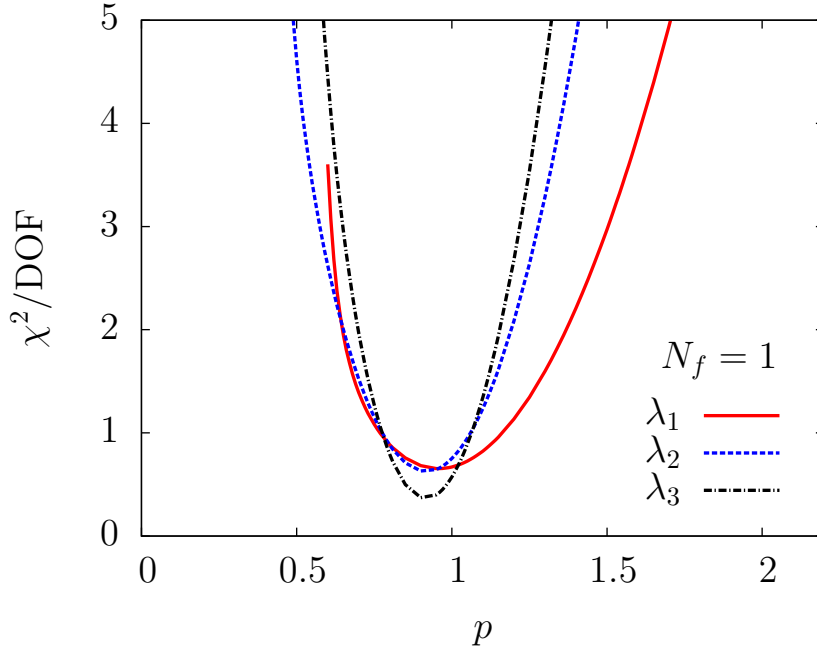


FIG. 5. The likelihood of the values of the exponent  $p$  describing the asymptotic behavior  $\lambda\ell \sim \ell^{-p}$ . The  $\chi^2/\text{DOF}$  for the fit of the ansatz in Eq. (21) to the  $\ell$ -dependence of the continuum extrapolated  $\lambda\ell$  is shown as a function of  $p$ . The degrees of freedom  $\text{DOF}=9$  for the fits. The three different curves correspond to the lowest three eigenvalues. The plot shows that  $p=2$ , which is expected when condensate is present, is excluded.

equation in [14]. Of course, one cannot define a condensate at zero momentum in the presence of an infra-red cutoff but one can ask if the gap equation has a non-trivial solution. It is argued in [29] that one need to have  $\ell > 200$  to obtain a non-trivial solution for  $N_f = 1$ . This argument is based on the assumption that the lowest momentum appearing in the fermion loop is  $\pi/\ell$ . If instead, we replace the sum over momenta in the fermion loop by a sum over the eigenvalues of the Dirac operator in the presence of a gauge field background, a more natural choice for the infra-red cutoff is the lowest eigenvalue  $\lambda_1$  which, in our simulations, behaves like  $1/\ell^2$ . Explicitly, at our largest physical extent  $\ell = 250$ ,  $\frac{1}{\lambda_1} \approx 500$  which is well inside the region for a non-trivial solution in [29].

### C. Comparison to non-chiral random matrix theory

We can provide further credence to our conclusion of an absence of a bilinear condensate at  $N_f = 1$  by borrowing ideas from random matrix theory. In a theory that has a non-zero bilinear condensate in three dimensions, we should find low-lying eigenvalues to scale like  $1/\ell^3$  and this behavior should extend for all eigenvalues below a threshold proportional to  $1/\ell^2$ . One expects these low-lying eigenvalues to be dependent only on the fluctuations of the zero-mode of the chiral Lagrangian, and hence determined only by the symmetries of the low-energy theory. Thus, a diminishing fraction of eigenvalues ( $\ell$  out of the  $\ell^3$  eigenvalues), should be described by a random matrix theory (RMT) which has the same symmetries as that of the Dirac operator (see Eq. (5)), but the actual number of them would get larger as one goes to infinite volume. This low-lying spectrum of eigenvalues is the ergodic regime. The non-chiral RMT which has the same symmetries as that of QED<sub>3</sub> has been studied in [26]. A consequence is that the ratios of eigenvalues must be universal and be described by this non-chiral RMT. In the top panel of Figure 6, we plot the histogram  $P(\lambda_1/\lambda_2)$  at various volumes. The expectation from RMT is also shown. A large volume dependence is seen. In order to take the  $\ell \rightarrow \infty$  limit, it was convenient for us to use the cumulant generating function  $G(s)$ ,

$$G(s) = \log \int_0^\infty P(x) e^{-sx} dx \quad \text{where} \quad x = \frac{\lambda_1}{\lambda_2}. \quad (22)$$

These are shown in the bottom panel of Figure 6. Using a [1/1] Padé approximant, we extrapolated the  $G(s)$  to its  $\ell \rightarrow \infty$  limit. This is shown by the green band, labelled  $\ell = \infty$ , in Figure 6. It is clear that there is no agreement with non-chiral RMT. Nevertheless, we note that the ratio  $\lambda_1/\lambda_2$  does have a non-trivial limit showing that the different eigenvalues scale the same way with volume. However this scaling is not  $1/\ell^3$ . This justifies the inference from Figure 5.

### D. Emergence of critical behavior

In the ergodic regime, the eigenmodes would be delocalized and the associated Inverse Participation Ratio (IPR),

$$I_2(\lambda) = \int (\psi_\lambda^*(x)\psi_\lambda(x))^2 d^3x \quad \text{with normalization} \quad \int \psi_\lambda^*(x)\psi_\lambda(x) d^3x = 1, \quad (23)$$

would scale as  $1/\ell^3$ . The IPR for the lowest mode is plotted in Figure 7. We see a significant deviation away from the ergodic behavior. Instead, the modes seem to be delocalized, but multi-

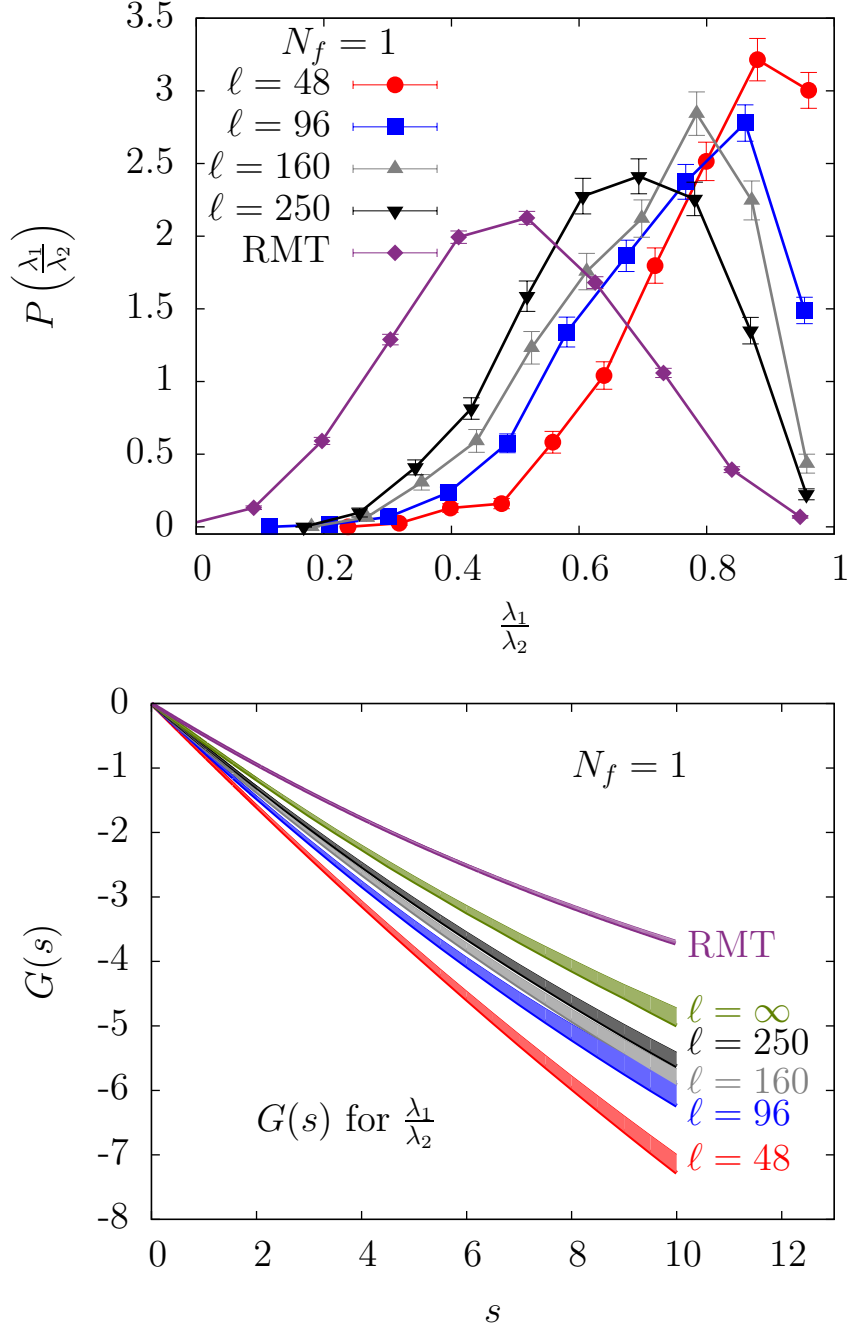


FIG. 6. Distribution of  $\lambda_1/\lambda_2$ . The top panel shows the histogram of  $\lambda_1/\lambda_2$  at various volumes. The magenta diamonds correspond to that of non-chiral random matrix theory. The bottom panel shows the  $1\text{-}\sigma$  bands of the cumulant generating function  $G(s)$  for the probability distributions in the top panel. The green band (labelled  $\ell = \infty$ ) is the infinite volume extrapolation of  $G(s)$ . The magenta band (labelled as RMT) is the expectation from non-chiral RMT.

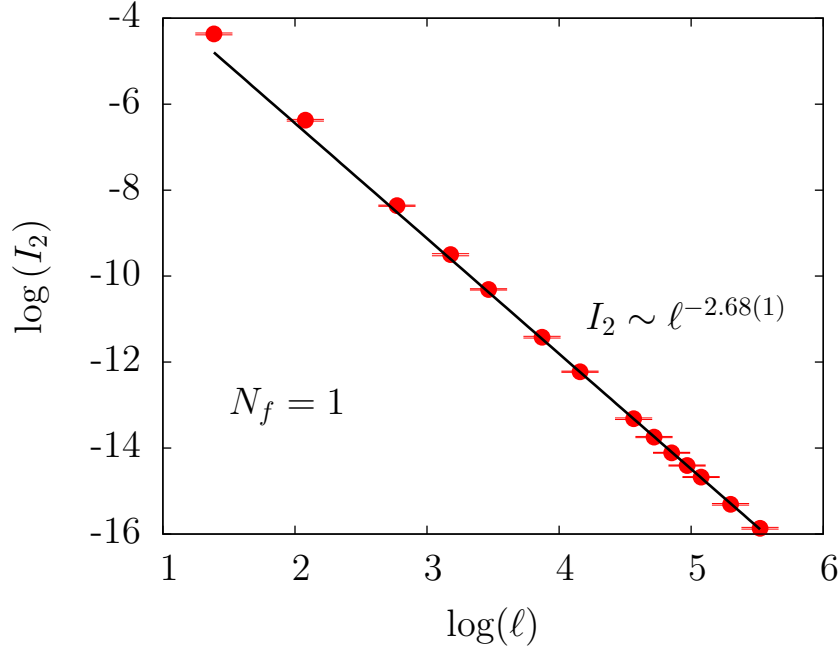


FIG. 7. A plot of the IPR of the lowest eigenmode as a function of the physical volume. The red circles are the data from our simulation. The black line is the power-law behaviour ( $I_2 \sim \ell^{-2.68}$ ) seen at large enough box sizes  $\ell$ . The ergodic behaviour would have been  $I_2 \sim \ell^{-3}$ .

fractal *i.e.*,

$$I_2(\ell) \sim \ell^{-3+\eta} \quad \text{with} \quad \eta \neq 0. \quad (24)$$

In our case, the value of  $\eta$  is 0.32(1). This multi-fractal scaling suggests a critical behavior, which is further quantified below. It is usual to draw analogy between the broken phase where an RMT description is possible and a metallic state [30]. In this spirit, this behavior of IPR is reminiscent of the behavior of electron wavefunction at a metal-insulator critical point.

We proceed to compare the behavior of the IPR of the lowest mode with that of number variance, a quantity that does not depend on the microscopic spectral density, but is a measure of ergodic behavior [30–33]. The number variance is computed as follows: having chosen a  $\lambda$ , we find the number of eigenvalues  $n$  below that scale per configuration. Then, the number variance is

$$\Sigma_2(n) = \text{Var}(n). \quad (25)$$

Normally, one wants to study this quantity in the bulk away from the edge such that critical

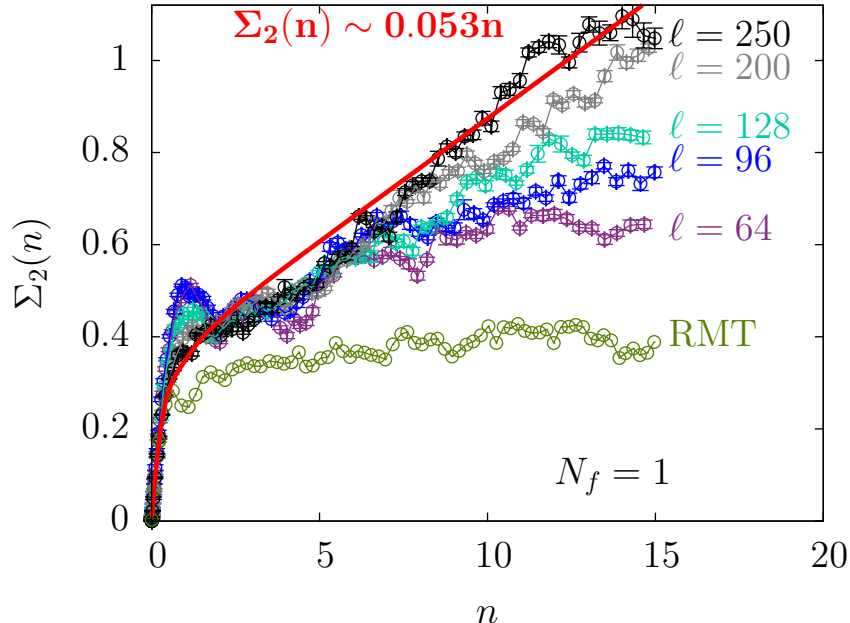


FIG. 8. A plot of the number variance  $\Sigma_2(n)$  as a function of  $n$ , the number of eigenvalues below a certain scale, for different physical volumes. The green points (labelled RMT) are the ones expected from non-chiral random matrix theory, which is ergodic. The red solid curve is obtained from the  $q$ -Hermite random matrix model (refer Eq. (30)), which is critical and has an asymptotic behavior  $\Sigma_2(n) \sim \chi n$ . The value of  $\chi$  was set to  $\eta/6 = 0.053$  as inferred from the  $\ell$ -dependence of IPR in Figure 7.

behavior sets in at the transition between the ergodic,

$$\Sigma_2(n) \sim \ln n, \quad (26)$$

and diffusive,

$$\Sigma_2(n) \sim n^{\frac{3}{2}}, \quad (27)$$

behavior. As noted earlier, the region showing the ergodic behavior should increase linearly with  $\ell$ . In Figure 8, we show the behavior of  $\Sigma_2(n)$  for several physical volumes. The behavior at large volumes show a linear rise over a wide range with no region that shows ergodic behavior (labelled as RMT). Furthermore, the slope of the linear growth,

$$\Sigma_2(n) = \chi n, \quad (28)$$

is  $\chi = 0.057$ , which is consistent with the critical relation [33]

$$\eta = 6\chi, \quad (29)$$

between the slope of the number variance and the multi-fractal dimension  $\eta$  of the lowest mode. This critical behavior seen right from the lowest mode is surprising. There are random matrix theory models with special choices of potentials where all states exhibit critical behavior [34]. An exactly solved model in this critical class of random matrix theories is the  $q$ -Hermite model introduced in [35], and it has a single tunable parameter, which is the slope  $\chi$  at large  $n$ . The number variance in the model is given by [36, 37]

$$\Sigma_2(n) = n - 2\pi^2\chi^2 \int_0^n (n - \xi) \left[ \frac{\sin(\pi\xi)}{\sinh(\pi^2\chi\xi)} \right]^2 d\xi, \quad (30)$$

which behaves asymptotically as  $\Sigma_2(n) \sim \chi n$ . We compare our data to that of the  $q$ -Hermite model as follows: using the value  $\eta = 0.32$  that we determined from the IPR of the lowest mode (refer Figure 7), we calculated the number variance for the  $q$ -Hermite model using the above equation with  $\chi = \eta/6$ . This is shown as the red solid curve in Figure 8. An agreement is seen, even for small  $n$  (with no fitting involved).

#### IV. RESULTS FOR $N_f > 1$

Our results for  $N_f > 1$  are provided with the aim of comparing them to the  $N_f = 1$  results. With that in mind, some of the previous plots are repeated for convenience to the reader. The behavior of the lowest eigenvalue as a function of the physical extent of the box,  $\ell$ , is shown in the top panel of Figure 9. Clearly, at any  $\ell$ , the value of the eigenvalue itself increases with  $N_f$ , and this is due to the suppression of the low eigenvalues by the fermion determinant. In addition, all the four cases show a behavior that is consistent with an absence of a bilinear condensate. The  $\chi^2$ -values for the different values of the exponent  $p$  which describes the asymptotic behavior  $\lambda_1\ell \sim \ell^{-p}$  (refer to Eq. (21)), is shown in the bottom panel of Figure 9. From this, we estimate the values of  $p$  to be  $0.97^{+0.34}_{-0.30}$ ,  $0.63^{+0.22}_{-0.15}$ ,  $0.37^{+0.05}_{-0.06}$  and  $0.28^{+0.05}_{-0.06}$  for  $N_f = 1, 2, 3$  and  $4$  respectively. The values of  $p$  seem to monotonically decrease with  $N_f$ . In fact, the trend seems to be consistent with  $p = \frac{1}{N_f}$  behavior.

In Figure 10, we compare the IPR of the lowest mode for  $N_f = 1$  (top left panel) to that of  $N_f = 2$  (top right),  $N_f = 3$  (bottom left) and  $N_f = 4$  (bottom right). The black lines are



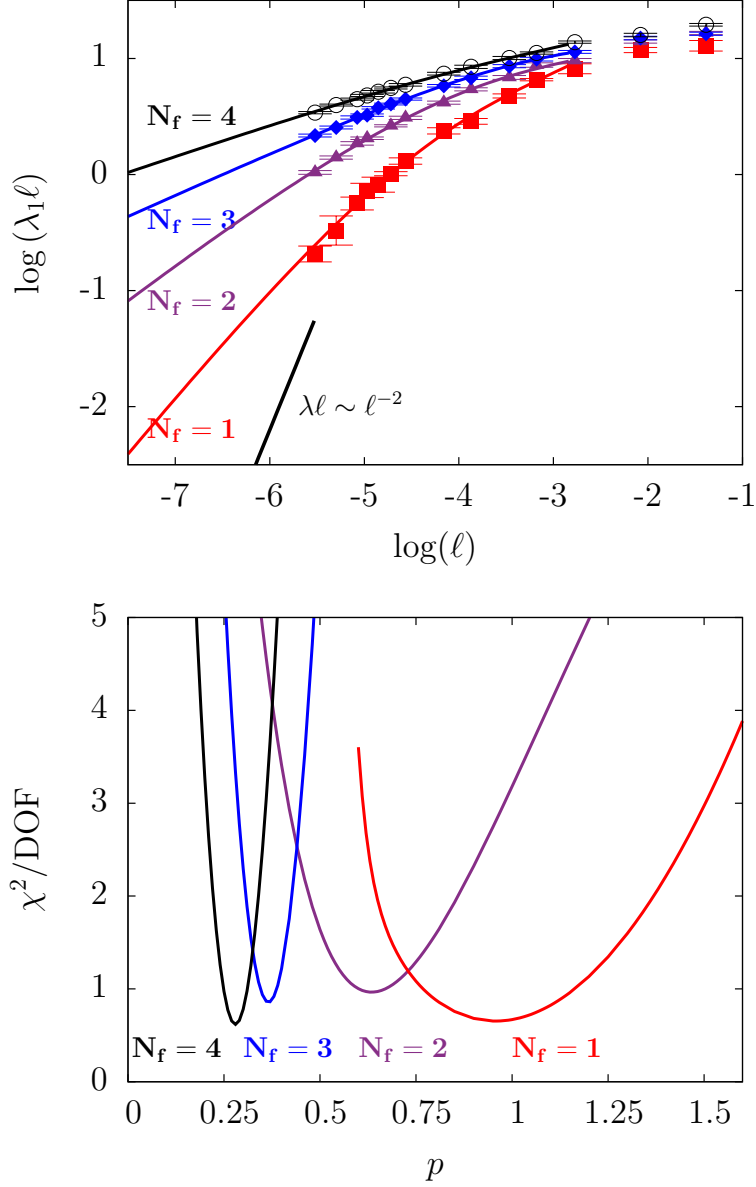


FIG. 9. The top panel shows the  $\ell$ -dependence of the continuum extrapolated dimensionless eigenvalue,  $\lambda_1 \ell$ , for  $N_f = 1, 2, 3, 4$  (as labelled on the left of the plot). The power-law  $\ell^{-2}$ , expected if a condensate is present, is shown for comparison. The different curves are the best fits of the finite volume ansatz in Eq. (21) to the data. The bottom panel shows the  $\chi^2/\text{DOF}$  for the fit of the finite volume ansatz to the data, as a function of exponent  $p$ , which describes the asymptotic behavior  $\lambda_1 \ell \sim \ell^{-p}$ . The most likely value of  $p$  seems to decrease monotonically with  $N_f$ .

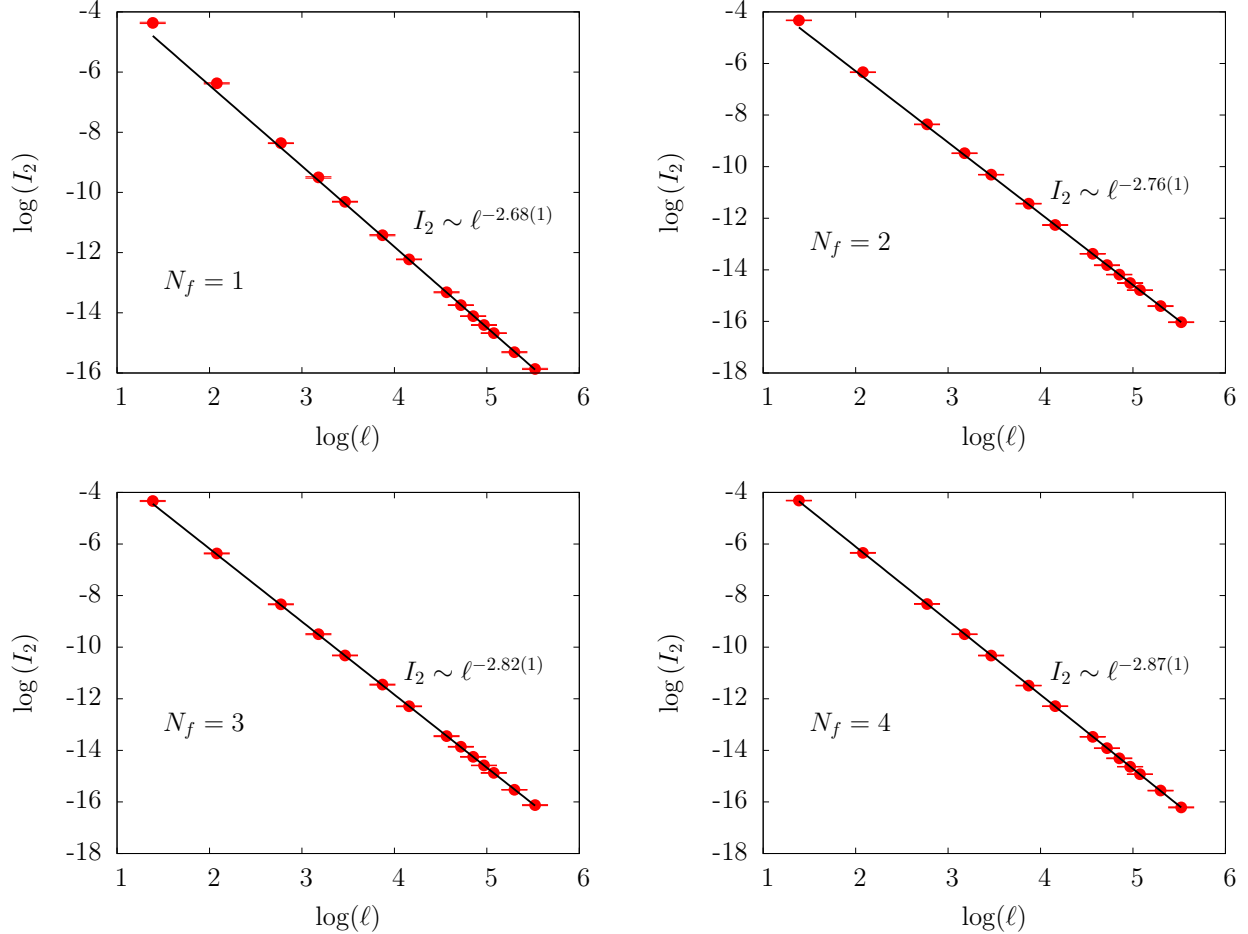


FIG. 10. A plot of the IPR,  $I_2$ , of the lowest eigenmode as a function of the physical extent of the box,  $\ell$ , for  $N_f = 1$  (top left),  $N_f = 2$  (top right),  $N_f = 3$  (bottom left) and  $N_f = 4$  (bottom right). The black lines are the best fits of the power law,  $I_2 \sim \ell^{-3+\eta}$ , to the IPR at large volumes.

the power-law fits,  $\ell^{-3+\eta}$ , to the data at large volumes. In all the four cases, we see systematic deviation away from the ergodic  $\ell^{-3}$  behavior; instead, we see a multi-fractal scaling at all  $N_f$ . The deviation from the ergodic behavior gets smaller as we increase  $N_f$ . In Figure 11, we compare the number variance of  $N_f = 1$  (top left panel) with that of  $N_f = 2$  (top right),  $N_f = 3$  (bottom left) and  $N_f = 4$  (bottom right) for different choices of physical volume. Let us first focus on the  $N_f = 2$  case. The signature of critical behavior is the linear rise of  $\Sigma_2(n)$ . The linear rise seen for  $N_f = 1$  is also present for  $N_f = 2$ . As explained in Section III, the number variance for the critical  $q$ -Hermite random matrix model, tuned to have an asymptotic behavior  $\Sigma_2(n) \sim \frac{\eta}{6}n$ , is also shown as a red solid curve. At the volumes we simulated, an agreement is not seen for

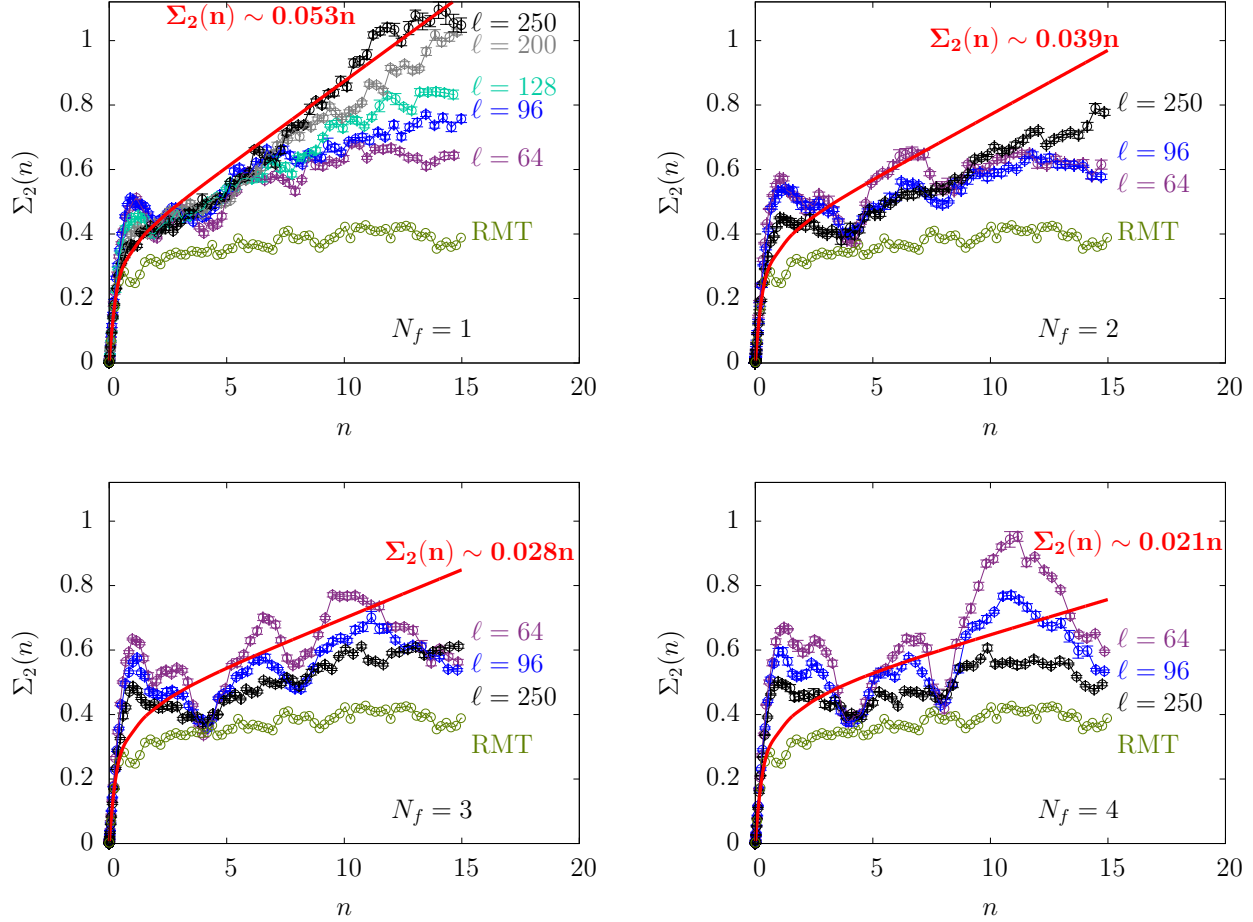


FIG. 11. A plot of the number variance for several different physical volumes for  $N_f = 1$  (top left),  $N_f = 2$  (top right),  $N_f = 3$  (bottom left) and  $N_f = 4$  (bottom right). The red solid curves are obtained from the  $q$ -Hermite random matrix model (refer Eq. (30)), tuned to have a behavior  $\Sigma_2(n) \sim \frac{\eta}{6}n$ , at large  $n$ , with  $\eta$  determined from the IPR of the lowest mode (refer Figure 10).

$N_f = 2$ . Nevertheless, the linear rise in  $\Sigma_2(n)$  approaches  $\eta/6$  at large volumes (as seen by comparing the slope of the linear rise in the data to that of the red solid curve). The trend in the data is for the linear segment of  $\Sigma_2(n)$  to shift upwards towards the critical random matrix model with increasing volume. To check if an agreement is seen at even larger physical volumes, requires lattices with larger  $L$  in order to control lattice artifacts. Such a computation is beyond the scope of this work. The presence of a possible linear rise for  $N_f = 3$  and  $N_f = 4$  is marred by an oscillatory behavior, perhaps because of the comparatively small value of slope as inferred from  $\eta$ .

## V. CONCLUSIONS

We have numerically studied a parity invariant formulation of QED in three dimensions using Wilson fermions. We investigated theories with 2, 4, 6 and 8 flavors of massless two component fermions. We used the behavior of low-lying eigenvalues of the four component Dirac operator to investigate the presence or absence of a bilinear condensate that preserves parity. Our computations were performed on several physical volumes and lattice spacings. The resulting low-lying spectrum did not exhibit a  $\ell^{-3}$  dependence on the physical linear extent,  $\ell$ , of the three-dimensional symmetric periodic box for any of the theories studied here. A study of the inverse participation ratio of the eigenvectors associated with the low-lying eigenvalues shows that the modes exhibit critical behavior when the scaling exponent was compared to the linear rise of the number variance associated with the low-lying eigenvalues. Furthermore, the agreement of the number variance for  $N_f = 1$  between a  $q$ -Hermite random matrix model and our data warrants further comparison with a critical random matrix model. For example, we plan to compare the distribution of low-lying eigenvalues of QED<sub>3</sub> with that of a critical random matrix model. We also plan to study non-abelian fields coupled to massless fermions. These theories are expected to be different since there is a non-vanishing string tension in pure gauge theories.

## ACKNOWLEDGMENTS

We would like to thank Shinsuke Nishigaki, Jac Verbaarschot and Rohana Wijewardhana for extensive discussions. R.N. would like to additionally thank Jac Verbaarschot for the invitation to the Simons Center Workshop on Random Matrix Theory, Integrable Systems, and Topology in Physics which resulted in useful discussions with Gernot Akemann, Takuya Kanzawa, Tamas Kovacs and Ismail Zahed. We would like to particularly thank Takuya Kanzawa for bringing [38] to our attention where the authors experimentally demonstrate that there is no gap in suspended graphene, a system where the low-lying modes are expected to be described by three-dimensional relativistic QED [1]. We would like to thank Khandker A. Muttalib for facilitating a quantitative comparison of our data with the  $q$ -Hermite random matrix model. All computations in this paper were made on the JLAB computing clusters under a class B project. The authors acknowledge partial support by the NSF under grant number PHY-1205396 and PHY-1515446.

**Appendix A: Details of the two component Sheikholami-Wohlert-Wilson-Dirac operator**

We are dealing with abelian gauge theory, therefore we smeared the gauge-fields  $\theta_i$  and then constructed the smeared links from them. Let the directions  $\hat{j}$  and  $\hat{k}$  be orthogonal to  $\hat{i}$ . Explicitly, the HYP smeared field  $\theta_i^s(n)$  is given by

$$\begin{aligned}
\theta_i^s(n) = s_2^2 & \left[ \frac{1}{4}\theta_i(n - \hat{j} - \hat{k}) + \frac{1}{4}\theta_i(n + \hat{j} - \hat{k}) + \frac{1}{4}\theta_i(n - \hat{j} + \hat{k}) + \frac{1}{4}\theta_i(n + \hat{j} + \hat{k}) \right. \\
& - \frac{1}{8}\theta_j(n + \hat{i} - \hat{k}) + \frac{1}{8}\theta_j(n + \hat{i} - \hat{j} - \hat{k}) - \frac{1}{8}\theta_j(n + \hat{i} + \hat{k}) + \frac{1}{8}\theta_j(n + \hat{i} - \hat{j} + \hat{k}) \\
& - \frac{1}{8}\theta_k(n + \hat{i} - \hat{j}) - \frac{1}{8}\theta_k(n + \hat{i} + \hat{j}) + \frac{1}{8}\theta_k(n + \hat{i} - \hat{j} - \hat{k}) + \frac{1}{8}\theta_k(n + \hat{i} + \hat{j} - \hat{k}) \\
& - \frac{1}{4}\theta_i(n - \hat{j}) - \frac{1}{4}\theta_i(n + \hat{j}) - \frac{1}{4}\theta_i(n - \hat{k}) - \frac{1}{4}\theta_i(n + \hat{k}) \\
& + \frac{1}{8}\theta_j(n - \hat{k}) - \frac{1}{8}\theta_j(n - \hat{j} - \hat{k}) + \frac{1}{8}\theta_j(n + \hat{k}) - \frac{1}{8}\theta_j(n - \hat{j} + \hat{k}) \\
& \left. + \frac{1}{8}\theta_k(n - \hat{j}) + \frac{1}{8}\theta_k(n + \hat{j}) - \frac{1}{8}\theta_k(n - \hat{j} - \hat{k}) - \frac{1}{8}\theta_k(n + \hat{j} - \hat{k}) \right] \\
& + s_1 \left[ \frac{1}{4}\theta_i(n - \hat{j}) + \frac{1}{4}\theta_i(n + \hat{j}) - \frac{1}{4}\theta_j(n + \hat{i}) + \frac{1}{4}\theta_j(n + \hat{i} - \hat{j}) \right. \\
& + \frac{1}{4}\theta_i(n - \hat{k}) + \frac{1}{4}\theta_i(n + \hat{k}) - \frac{1}{4}\theta_k(n + \hat{i}) + \frac{1}{4}\theta_k(n + \hat{i} - \hat{k}) - \theta_i(n) \\
& \left. + \frac{\theta_j(n)}{4} - \frac{1}{4}\theta_j(n - \hat{j}) + \frac{\theta_k(n)}{4} - \frac{1}{4}\theta_k(n - \hat{k}) \right] + \theta_i(n). \tag{A1}
\end{aligned}$$

We set the smearing parameters to  $s_1 = 0.6$  and  $s_2 = 0.5$ . The unsmeared and smeared link variables are given by

$$U_i(n) = e^{i\theta_i(n)} \quad \text{and} \quad V_i(n) = e^{i\theta_i^s(n)}, \tag{A2}$$

respectively. The Sheikholami-Wohlert-Wilson-Dirac operator for the two-component fermion, in lattice units, is

$$\begin{aligned}
C_W(n, m) = & (-3 + M_P)\delta_{n,m} + \frac{1}{2} \sum_{i=1}^3 \left\{ (1 + \sigma_i) V_i(n)\delta_{n+i,m} + (1 - \sigma_i) V_i^*(n - \hat{i})\delta_{n-i,m} \right\} \\
& + i \frac{\kappa_{SW}}{8} \delta_{n,m} \sum_{i,j,k=1}^3 \epsilon_{ijk} C_{ij}(n) \sigma_k, \tag{A3}
\end{aligned}$$

where the clover term is

$$C_{ij}(n) = P_{ij}(n) + P_{ij}(n - \hat{i}) + P_{ij}(n - \hat{j}) + P_{ij}(n - \hat{i} - \hat{j}), \tag{A4}$$

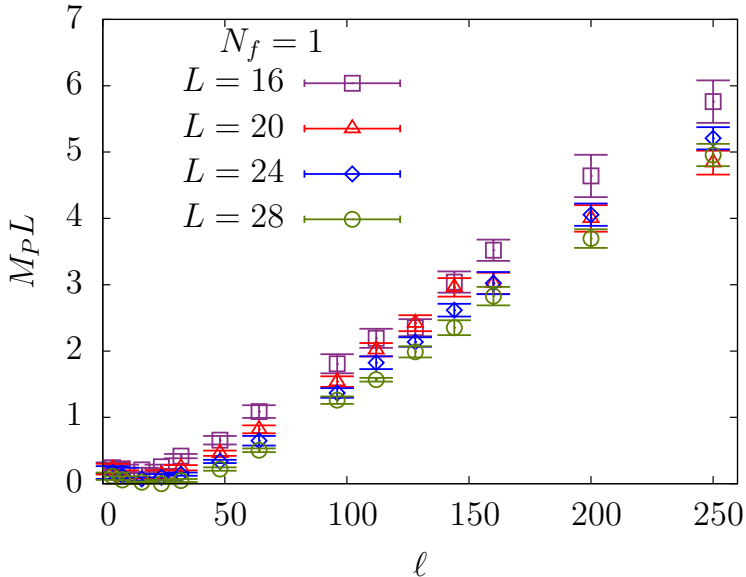


FIG. 12. The tuned mass in physical units,  $M_P L$ , is shown as a function of  $\ell$  at different lattice sizes  $L$ .

in terms of the plaquette,

$$P_{ij}(n) = U_i(n)U_j(n + \hat{i})U_i^*(n + \hat{j})U_j^*(n). \quad (\text{A5})$$

We used the value  $\kappa_{SW} = 0.5$  at all  $\ell$  and  $L$ . Using these values of  $\kappa_{SW}$  and the smearing parameters,  $s_1$  and  $s_2$ , we found the additive mass renormalization to be greatly reduced even in our coarsest lattices.

## Appendix B: Simulation details

The free parameters are the physical extent of the box,  $\ell$ , the lattice size,  $L$ , the tuned Wilson mass,  $M_P$ , and the number of flavors,  $N_f$ . We used  $N_f = 1, 2, 3$  and  $4$  in our simulations. The continuum limit is taken by taking  $L \rightarrow \infty$  keeping  $\ell$  fixed. For this, we used  $L = 16, 20, 24$  and  $28$  lattices. At any finite  $L$ , the additive renormalization of fermion mass is taken care of by tuning  $M_P$ . Since QED<sub>3</sub> is super-renormalizable,  $M_P L$  is a finite additive renormalization. We tabulate the simulation parameters for the  $N_f = 1$  data set in Table I. We also show  $M_P L$  as a function of  $\ell$  graphically in Figure 12. We used the same set of  $\ell$  for  $N_f = 2, 3$  and  $4$  as well.

In the HMC simulation, we kept the molecular dynamics step-size  $\Delta t$  to be  $1/N_{MD}$ . We tuned

$\ell$	$M_P$			
	$L = 16$	$L = 20$	$L = 24$	$L = 28$
4	0.015(5)	0.011(4)	0.007(4)	0.006(3)
8	0.014(4)	0.005(5)	0.006(2)	0.002(2)
16	0.013(2)	0.003(1)	0.003(1)	0.0008(4)
24	0.016(2)	0.007(3)	0.004(2)	0.000(2)
32	0.026(2)	0.012(2)	0.006(1)	0.0017(8)
48	0.041(4)	0.023(2)	0.014(1)	0.0079(9)
64	0.068(6)	0.041(3)	0.027(3)	0.018(1)
96	0.113(9)	0.077(4)	0.057(3)	0.045(2)
112	0.137(9)	0.101(5)	0.076(4)	0.056(1)
128	0.147(8)	0.121(6)	0.089(3)	0.071(3)
144	0.19(1)	0.148(7)	0.109(4)	0.084(4)
160	0.22(1)	0.151(8)	0.126(7)	0.101(5)
200	0.29(2)	0.20(1)	0.169(7)	0.132(5)
250	0.36(2)	0.242(9)	0.217(7)	0.177(6)

TABLE I. Simulation parameters for  $N_f = 1$ .

the number of steps per trajectory,  $N_{\text{MD}}$ , at run time to keep the Monte Carlo acceptance near 80%. At all simulation points, we ran about 13,500 trajectories with the first 300 trajectories discarded for thermalization. Then, we used only the gauge configurations separated by an autocorrelation time,  $\tau$ , as determined from the smallest eigenvalue of the Dirac operator.

- 
- [1] V. A. Miransky and I. A. Shovkovy, Phys. Rept. **576**, 1 (2015), arXiv:1503.00732 [hep-ph].
  - [2] S. Deser, R. Jackiw, and S. Templeton, Annals Phys. **140**, 372 (1982).
  - [3] S. Deser, R. Jackiw, and S. Templeton, Phys.Rev.Lett. **48**, 975 (1982).
  - [4] A. Niemi and G. Semenoff, Phys.Rev.Lett. **51**, 2077 (1983).
  - [5] A. Redlich, Phys.Rev. **D29**, 2366 (1984).
  - [6] H. So, Prog.Theor.Phys. **73**, 528 (1985).

- [7] H. So, Prog.Theor.Phys. **74**, 585 (1985).
- [8] A. Coste and M. Luscher, Nucl.Phys. **B323**, 631 (1989).
- [9] S. Deser, L. Griguolo, and D. Seminara, Phys.Rev. **D57**, 7444 (1998), arXiv:hep-th/9712066 [hep-th].
- [10] N. Karthik and R. Narayanan, Phys. Rev. **D92**, 025003 (2015), arXiv:1505.01051 [hep-th].
- [11] R. D. Pisarski, Phys.Rev. **D29**, 2423 (1984).
- [12] T. Appelquist, M. J. Bowick, E. Cohler, and L. C. R. Wijewardhana, Phys. Rev. Lett. **55**, 1715 (1985).
- [13] T. W. Appelquist, M. J. Bowick, D. Karabali, and L. C. R. Wijewardhana, Phys. Rev. **D33**, 3704 (1986).
- [14] T. Appelquist, M. J. Bowick, D. Karabali, and L. C. R. Wijewardhana, Phys. Rev. **D33**, 3774 (1986).
- [15] T. Appelquist, D. Nash, and L. C. R. Wijewardhana, Phys. Rev. Lett. **60**, 2575 (1988).
- [16] T. Appelquist, A. G. Cohen, and M. Schmaltz, Phys. Rev. **D60**, 045003 (1999), arXiv:hep-th/9901109 [hep-th].
- [17] S. Giombi, I. R. Klebanov, and G. Tarnopolsky, (2015), arXiv:1508.06354 [hep-th].
- [18] S. Hands, J. Kogut, and C. Strouthos, Nucl.Phys. **B645**, 321 (2002), arXiv:hep-lat/0208030 [hep-lat].
- [19] S. Hands, J. Kogut, L. Scorzato, and C. Strouthos, Phys.Rev. **B70**, 104501 (2004), arXiv:hep-lat/0404013 [hep-lat].
- [20] O. Raviv, Y. Shamir, and B. Svetitsky, Phys. Rev. **D90**, 014512 (2014), arXiv:1405.6916 [hep-lat].
- [21] S. Hands and J. B. Kogut, Nucl. Phys. **B335**, 455 (1990).
- [22] B. Sheikholeslami and R. Wohlert, Nucl. Phys. **B259**, 572 (1985).
- [23] A. Hasenfratz and F. Knechtli, Phys. Rev. **D64**, 034504 (2001), arXiv:hep-lat/0103029 [hep-lat].
- [24] A. Hasenfratz, R. Hoffmann, and S. Schaefer, JHEP **05**, 029 (2007), arXiv:hep-lat/0702028 [hep-lat].
- [25] T. Banks and A. Casher, Nucl. Phys. **B169**, 103 (1980).
- [26] J. J. M. Verbaarschot and I. Zahed, Phys. Rev. Lett. **73**, 2288 (1994), arXiv:hep-th/9405005 [hep-th].
- [27] S. Duane, A. Kennedy, B. Pendleton, and D. Roweth, Phys.Lett. **B195**, 216 (1987).
- [28] T. Kalkreuter and H. Simma, Comput. Phys. Commun. **93**, 33 (1996),



arXiv:hep-lat/9507023 [hep-lat].

- [29] V. P. Gusynin and M. Reenders, Phys. Rev. **D68**, 025017 (2003), arXiv:hep-ph/0304302 [hep-ph].
- [30] J. C. Osborn and J. J. M. Verbaarschot, Nucl. Phys. **B525**, 738 (1998), arXiv:hep-ph/9803419 [hep-ph].
- [31] B. Al'tschuler and B. Shklovskii, Sov. Phys. JETP **64**, 127 (1986).
- [32] B. Al'tschuler, I. Zharekeshev, S. Kotochigova, and B. Shklovskii, Sov. Phys. JETP **67**, 625 (1988).
- [33] V. Chalker, J.T. and Kravtsov and I. Lerner, Pis'ma v ZhETF **64**, 355 (1996).
- [34] V. E. Kravtsov and K. A. Muttalib, Phys. Rev. Lett. **79**, 1913 (1997).
- [35] K. A. Muttalib, Y. Chen, M. E. H. Ismail, and V. N. Nicopoulos, Phys. Rev. Lett. **71**, 471 (1993).
- [36] C. Blecken, Y. Chen, and K. A. Muttalib, J. Phys. A: Math. Gen. **27**, L563 (1994).
- [37] K. A. Muttalib, private communication.
- [38] D. Elias, R. Gorbachev, A. Mayorov, S. Morozov, A. Zhukov, P. Blake, L. Ponomarenko, I. Grigorieva, K. K. S. Novoselov, F. Guinea, and A. Geim, Nature Physics **7**, 701 (2011).